Theoretical investigation of pulse-to-pulse instabilities in synchronously pumped femtosecond optical parametric oscillator

VIKTORIJA TAMULIENĖ[1,*], MIKAS VENGRIS[1], AND VALDAS SIRUTKAITIS[1]

[1] Laser Research Center, Vilnius University, Saulėtekio 10, Vilnius LT-10223, Lithuania
[*] Corresponding author: viktorija.tamuliene@ff.vu.lt

Compiled December 16, 2019

Singly resonant synchronously pumped optical parametric oscillator (SPOPO) based on the experimental set-up of K. Ivanauskienė et. al. (2019) [1] is studied theoretically. Stable, oscillatory and chaotic operation modes of the SPOPO are investigated. The need of the self- and cross-phase modulation terms in the theoretical model for the explanation of the instabilities is demonstrated. The theoretical values of the wavelengths of the signal spectrum maxima are found. The evidence of chaos by the calculation of the Lyapunov exponent is provided. The possibilities to avoid the instabilities are discussed.

OCIS codes: (190.0190) Nonlinear optics; (190.4970) Parametric oscillators and amplifiers; (190.3100) Instabilities and chaos.

http://dx.doi.org/10.1364/ao.XX.XXXXXX

1. INTRODUCTION

Optical parametric oscillator (OPO) is a versatile tool providing light in near- and mid-infrared frequencies. At high pulse repetition rate and relatively low pulse energies, synchronously pumped OPOs are utilised [2] and the signal generated by SPOPO acquires high intensity. Recently, the oscillations and instabilities in singly resonant SPOPO were studied in [1]. The chaos in OPO operation has been discovered [3] and the oscillatory solutions were numerically obtained for SPOPOs [4]. However, accurate theoretical description of chaotic and oscillatory SPOPO behavior remains a challenge. As we will see in this study, the inclusion of the third-order nonlinear terms into the model is necessary.

The models of SPOPO including third order nonlinearities have been presented in [5], [6], [7]. In [5], the sech-type soliton solutions were found and the pulse broadening [6] as well as asymmetry [7] due to the self- and cross-phase modulations were observed. However, oscillatory behaviour was not observed in these studies. We note, that at some circumstances, the complex Ginzburg-Landau equation (CGLE) from the singly resonant SPOPO model can be derived [5]. The chaotic dissipative soliton solutions of CGLE were presented in [8].

In this paper, we study theoretically the stable as well as oscillatory and chaotic operations of singly resonant SPOPO based on BBO nonlinear crystal. In most practical situations, chaotic operation of SPOPO is undesirable. Therefore, this study should reveal the conditions at which the instabilities can be avoided. The model and its parameters are based on the recently described experimental implementation [1].

The rest of the paper includes Section 2, where the model equations of the SPOPO are described. In Section 3, we consider the stable operation of SPOPO and find the solutions for the wavelengths of the signal spectrum maxima. In Section 4, unstable operation is described and the evidence of the presence of chaos is provided. Conclusions are drawn in Section 5.

2. MODEL OF THE SINGLY RESONANT SPOPO

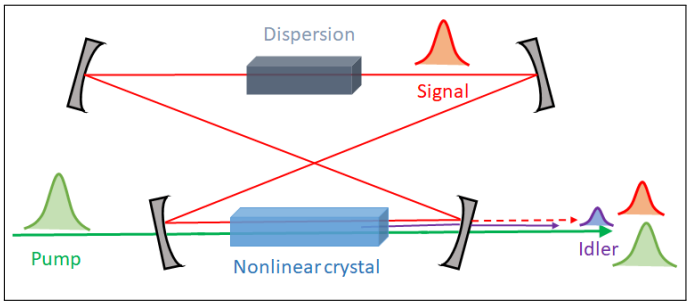

Fig. 1. (Color online) Schematic depiction of the singly resonant SPOPO.

We consider the three-wave interaction in the nonlinear type I BBO crystal that is placed inside the resonator, Fig. 1. The equations for the Fourier transforms $S_j(\Omega, z)$ of the electric fields $E_j(t, z)$ of the signal (index $j = 1$), idler (2) and pump (3) waves are given by [9]:

$$\frac{\partial S_1}{\partial z} = ik_1' S_1 + \sigma_1 \widehat{P}_1^{(2)} + i\gamma_1 \widehat{P}_1^{(3)}, \quad \textbf{(1a)}$$

$$\frac{\partial S_2}{\partial z} = ik_2' S_2 + \sigma_2 \widehat{P}_2^{(2)} + i\gamma_2 \widehat{P}_2^{(3)}, \quad \textbf{(1b)}$$

$$\frac{\partial S_3}{\partial z} = ik_3' S_3 - \sigma_3 \widehat{P}_3^{(2)} + i\gamma_3 \widehat{P}_3^{(3)}, \quad \textbf{(1c)}$$

where $z \in [0\ L]$ is the longitudinal coordinate, L is the crystal length. In $E_j(t, z)$, t is the time variable. The three terms at the right hand side of Eqs. (1) describe dispersion, second- and third- order nonlinearities. Next, we discuss each of them.

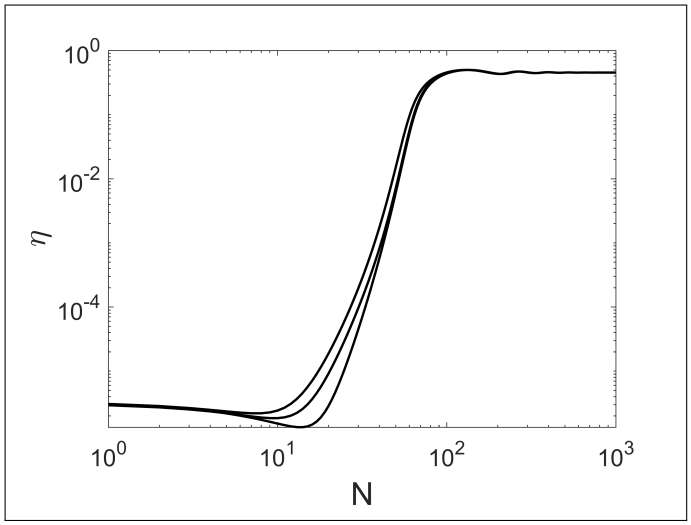

Fig. 2. Dependence of the conversion efficiency to the signal wave on the round-trip number. Stable operation. $E_{30} = 4$ nJ, $G_0 = -400$ fs^2, $l = 0$. Three different noise realizations.

1. Dispersion. In the time domain, the dispersion is described by the first order time derivative – the time walk-off – as well as by the second order time derivative – the group velocity dispersion – and the higher order derivatives [10]. The Fourier transform of the infinite series $\left(ik(\omega_0) - \frac{\partial k}{\partial \omega_0}\frac{\partial}{\partial t} - \frac{i}{2}\frac{\partial^2 k}{\partial \omega_0^2}\frac{\partial^2}{\partial t^2} + ...\right) E(t, z)$ is $i\left(k(\omega_0) + \Omega\frac{\partial k}{\partial \omega_0} + \frac{1}{2}\Omega^2\frac{\partial^2 k}{\partial \omega_0^2} + ...\right) S(\Omega, z) = ik(\omega_0 + \Omega)S(\Omega, z)$, where k is the wavelength-dependent wavenumber, $\omega_0 = 2\pi c/\lambda_0$ is the central angular frequency, c is speed of light, λ_0 is the central wavelength. For the j-th wave, $k_j' = k_j - \Omega/u_{10}$, $k_j = 2\pi n_j(\lambda_j)/\lambda_j$, where n_j is the refractive index found by the use of the Sellmeier's equations [11] and u_{10} is defined below. The phase matching conditions for the type I interaction are taken into account:

$$k_1(\omega_{10}) + k_2(\omega_{20}) = k_3(\omega_{30}), \quad \textbf{(2a)}$$

$$\omega_{10} + \omega_{20} = \omega_{30}. \quad \textbf{(2b)}$$

By the use of Eqs. (2) we find the phase-matching angle. The term Ω/u_{10} is subtracted from the wavenumber where $u_{10} = \left(\frac{\partial k_1}{\partial \omega}|_{\omega=\omega_{10}}\right)^{-1}$ is the group velocity of the signal wave. The propagation is described in the reference frame of the signal wave.

2. Second order nonlinearity. In Eqs. (1), the terms $\widehat{P}_j^{(2)}$ describe the three wave interaction. They are given by the inverse Fourier transforms of $E_3E_2^*$, $E_3E_1^*$ and E_1E_2 for the signal, idler and pump waves, respectively. The nonlinear coupling coefficient is given by $\sigma_j = \frac{2\pi d_{\text{eff}}}{n_{j0}\lambda_{j0}}$, where d_{eff} is the effective nonlinear coefficient.

3. Third order nonlinearity. $\widehat{P}_j^{(3)}$ is the Fourier transform of the nonlinear Kerr and XPM terms, e.g. in the time domain, $P_1^{(3)} = |E_1|^2E_1 + 2|E_2|^2E_1 + 2|E_3|^2E_1$. As we will see in Section 4, these terms influence the appearance of the oscillating and chaotic behaviour. The nonlinear coupling coefficient is given by $\gamma_j = n_2^{(I)}\frac{2\pi}{\lambda_{j0}}\frac{I_{30}}{|a_3|^2}$, where $n_2^{(I)}$ is the nonlinear refractive index, I_{30} is the input pump intensity and a_3 is the pump amplitude that will be introduced in Eq. (3c).

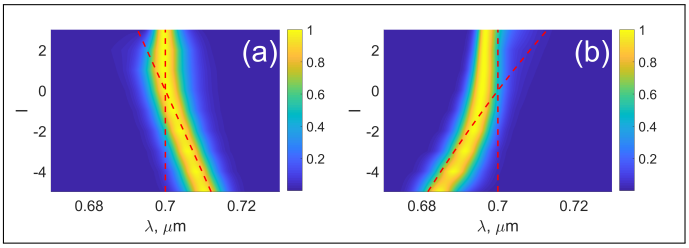

Fig. 3. (Color online) Dependence of the output signal spectra profiles on the time delay parameter l. Stable operation. $E_{30} = 4$ nJ, $N = 1000$. $G_0 = -400$ fs^2 ($G_s = G_0 + G_c < 0$) (a) and $G_0 = -200$ fs^2 ($G_s > 0$) (b). Dashed lines: $\Omega = 0$ and $\Omega = \Omega_0$, Eq. (7).

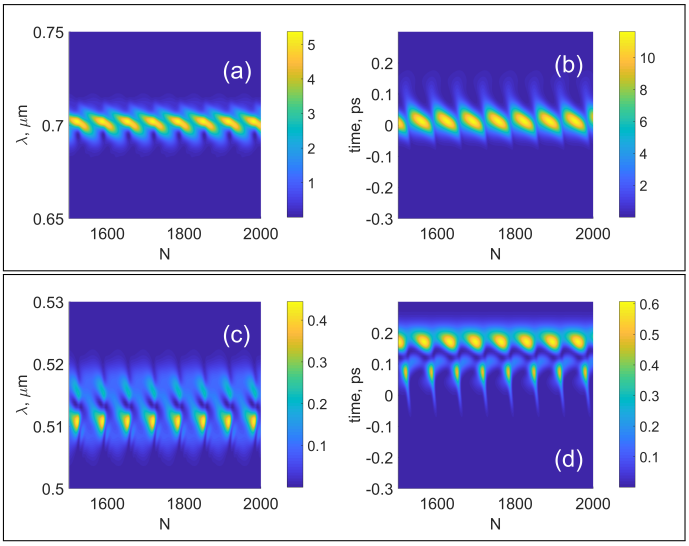

Fig. 4. (Color online) Dependence of the signal (a,b) and pump (c,d) spectrum (a,c) and temporal (b,d) profiles on the round-trip number. The intensity is normalized to the intensity of the input pump pulse. $z = L$, inside the resonator. $E_{30} = 6$ nJ, $l = 0$, $G_0 = -400$ fs^2.

At first round-trip $N = 1$ and $z = 0$ the boundary conditions

read

$$E_1(t,0) = a_0\xi_1(t), \tag{3a}$$
$$E_2(t,0) = 0, \tag{3b}$$
$$E_3(t,0) = a_3 \exp\left(-2\ln(2)\frac{t^2}{\tau^2}\right). \tag{3c}$$

The field ξ_1 is the random field of normal distribution with zero mean and variance that equals to unity. a_0 and a_3 are the amplitudes and τ is the pump pulse duration at FWHM. The input signal is the noise field and the pump wave is the Gaussian pulse.

At the end of the crystal, the transformations are applied:

$$S_1(\Omega,0)|_{N+1} = R^{1/2}S_1(\Omega,L)|_N \exp(i\varphi(\Omega)), \tag{4a}$$
$$S_2(\Omega,0)|_{N+1} = 0, \tag{4b}$$
$$S_3(\Omega,0)|_{N+1} = S_3(\Omega,0)|_{N=1}, \tag{4c}$$

where R is the reflectivity of the output mirror. Phase $\varphi(\Omega)$ is given by

$$\varphi(\Omega) = \delta\Omega + \frac{G_0}{2}\Omega^2, \tag{5}$$

where the time delay $\delta = l\lambda_{10}/(2c)$, l is the nondimensional number [12], G_0 is the group delay dispersion (GDD) predefined by the additional dispersive element inside the resonator, Fig. 1. The signal pulse is reflected by the output mirror, the idler leaves the resonator and the pump pulse is synchronously repeated at each round-trip.

Eqs. (1) were simulated by the use of the Fourier split-step method [13] for N round-trips. The crystal length was divided into 25 steps and the time window $[-10\tau, 10\tau)$ was divided into 256 steps. At each longitudinal step, Runge-Kutta method for the nonlinear part as well as fast Fourier transform for the linear part was applied. The parameters used in the simulation are the following: $\tau = 100$ fs, $L = 3$ mm, $R = 1 - 0.08$, $a_0/a_3 = 0.001$. As in the experimental work [1], pump wavelength $\lambda_{30} = 513$ nm and the crystal was phase-matched at $\lambda_{10} = 700$ nm. At these conditions, the crystal GDD $G_c = 275$ fs^2 and it is positive. The pump intensity I_{30} was calculated at various pump energies E_{30} assuming Gaussian beam with the beam radius of $d = 50$ μm.

3. STABLE OPERATION OF THE SPOPO

The typical dependence of the conversion efficiency to the signal wave $\eta = E_1/E_{30}$ is depicted in Fig. 2. Three different noise realizations of the input signal wave (Eq. (3a)) were applied. In the logarithmic scale, one can see the difference at the transient stage. At sufficiently large round-trip number N, all three curves saturate at the same value. Here, the net resonator GDD is negative: $G_s = (G_0 + G_c) < 0$. In Fig. 3, we compare the output signal spectrum profiles at the negative (Fig. 3a) and positive (Fig. 3b) net GDDs. At $l < 0$, the spectrum is shifted either to larger or smaller wavelengths. The shift can be found by the use of the following equation:

$$\frac{\partial\Delta\varphi}{\partial\Omega} = 0, \tag{6}$$

where $\Delta\varphi = \delta\Omega + \frac{1}{2}(G_0 + G_c)\Omega^2 + \frac{h}{6}\Omega^3$ is the net phase shift of the signal wave and $h = \frac{\partial^3 k_1}{\partial\omega_{10}^3}L$. From Eq. (6) we find

$$\Omega_0 = (-G_s + \mathrm{sign}(G_s)[|G_s|^2 - 2h\delta]^{1/2})/h. \tag{7}$$

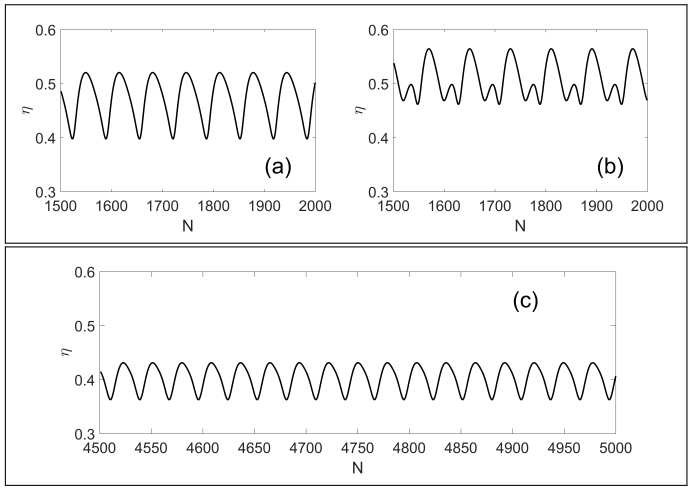

Fig. 5. Dependence of the conversion efficiency to the signal wave on the round-trip number. $G_0 = -400$ fs^2. (a): $E_{30} = 6$ nJ, $l = 0$, (b): $E_{30} = 8$ nJ, $l = 0$, (c): $E_{30} = 10.5$ nJ, $l = -3$.

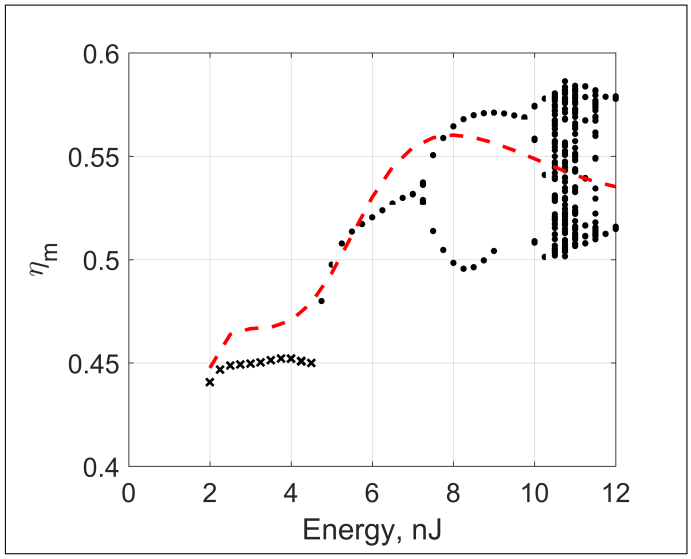

Fig. 6. (Color online) Poincaré map. Crosses: stable solutions, circles: maxima of oscillations. Dashed line: solutions of Eqs. (1) without self- and cross-phase modulation terms (only stable solutions). $G_0 = -400$ fs^2, $l = 0$.

This solution as well as $\Omega = 0$ are presented by the dashed line in Fig. 3.

At $h \approx 0$, $\Omega_0 \approx -\delta/G_s$. We see that the wavelength shift depends on the sign of G_s. Solution (7) can be explained by the fact that at $\Omega \approx \Omega_0$, the phase shift $\Delta\varphi$ becomes parabolic and there is no time walk-off. Another solution, $\Omega = 0$, corresponds to the condition $\Delta\varphi = 0$ that was considered in [12] where the singly resonant SPOPO was studied.

4. OSCILLATIONS AND CHAOS IN THE SPOPO

The oscillatory behaviour of the SPOPO was observed in the experimental work [1]. Typical one-period oscillations in spectrum as well as temporal profiles of the signal and pump pulses are visible from Fig. 4. By 'one-period' we mean that there is only one maximum value of the oscillating conversion efficiency η,

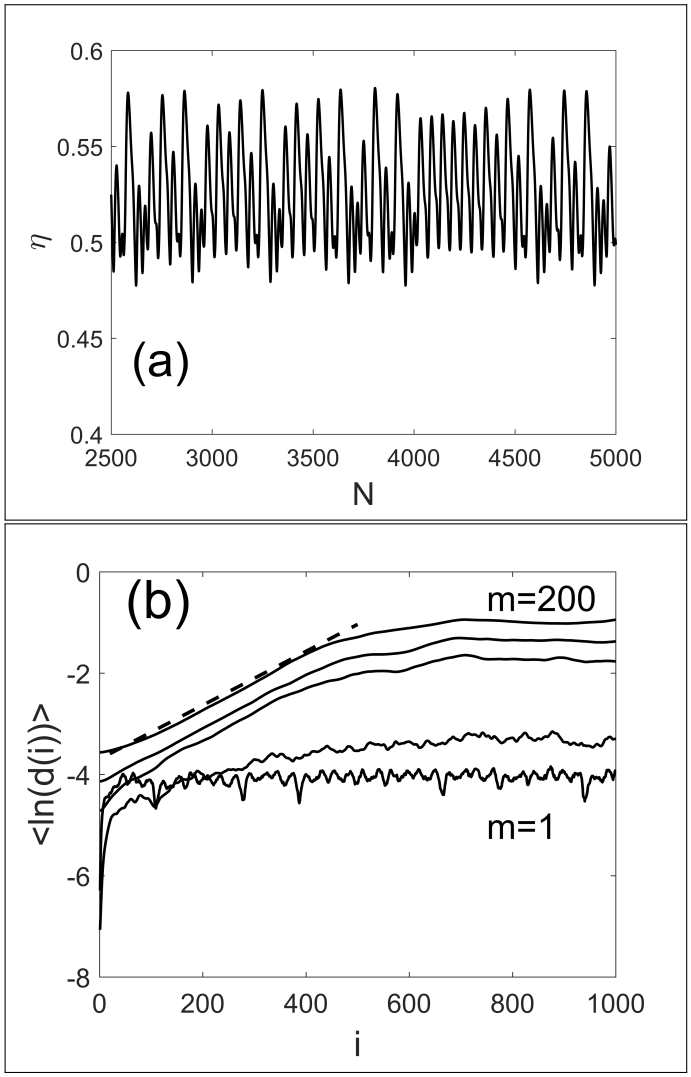

Fig. 7. (a) Dependence of the conversion efficiency on the round-trip number and (b) calculation of the Lyapunov exponent of the given data set by the use of the algorithm of [14]. Lag is equal to 1 and the embedded dimension m (from bottom to upper line): 1, 5, 50, 100, 200. d is the distance between the j-th pair of nearest neighbours after i discrete 'time' steps and brackets $\langle ... \rangle$ denote the averaging over all j [14]. $E_{30} = 10.5$ nJ, $G_0 = -400$ fs^2, $l = 0$.

see Fig. 5a. When the pump energy increases, the period doubling takes place and there are two maxima in Fig. 5b. We note that the oscillation period may change when the parameters are varied. For example, in Fig. 5c the period is twice smaller than the period in Fig. 5a. Here, the pump energy and parameter l values are different.

Dependence of maximum values η_m on pump energy E_{30} gives us the so called Poincaré map, Fig. 6. Here, the stable solutions (crosses) transform to the oscillating solutions (circles) at about 4.5 nJ. Increasing the energy the period doubling takes place. This is the well known Feigenbaum-type route to chaos. The evidence of chaos is a positive Lyapunov exponent. In the case of the chaotic sequence of Fig. 7a, we calculated the Lyapunov exponent by the use of the algorithm of Rosenstein et. al. [14]. This method is devoted to calculate the maximum

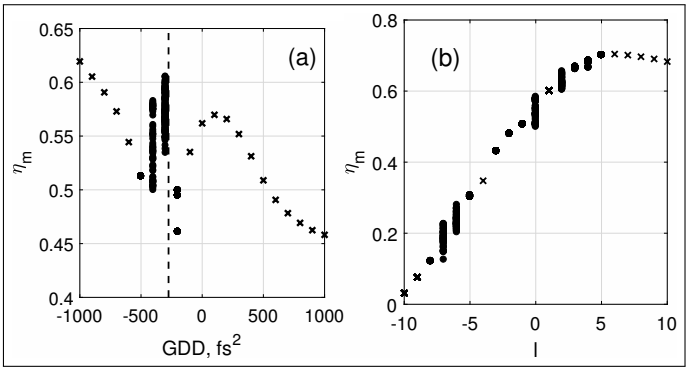

Fig. 8. Poincaré maps. Crosses: stable solutions, circles: maxima of oscillations. Dashed line in the (a): $G_s = G_0 + G_c = 0$. (a): $l = 0$, (b): $G_0 = -400$ fs^2. $E_{30} = 10.5$ nJ.

Lyapunov exponent from the available experimental time series. The Lyapunov exponent is given by the tangent of the dashed line in Fig. 7b. At sufficiently high value of the embedded dimension m, the tangent does not depend on m and it is positive. So, the positive Lyapunov exponent is an evidence of the chaos.

We note that the route to chaos can be obtained only with inclusion of the self- and cross-phase modulation terms in Eqs. (1). We repeated the simulations without these terms and obtained only stable solutions that are presented in Fig. 6 by the dashed line. We note that the oscillatory solutions are possible without inclusion of the $\chi^{(3)}$ term [4], but the chaotic behaviour does not occur.

In Fig. 8, two other Poincaré maps are depicted. At fixed l, the oscillatory and chaotic modes are obtained only at the vicinity of zero net GDD, $G_s = G_0 + G_c = 0$, dashed line in Fig. 8a. Large conversion efficiency and stable solutions are obtained at sufficiently large negative GDD. At fixed GDD, the stable solutions with large conversion efficiency were obtained at positive detuning parameter l, Fig. 8b. At fixed $l = 0$, the results are summarized in Fig. 9 where the two-parameter bifurcation diagram is shown. The diagram elucidates that the oscillatory and unstable modes are observed at larger pump energies at the vicinity of zero net GDD. The larger the energy the broader the range of GDDs.

In the recent experimental paper [15], the oscillatory as well as chaotic SPOPO operation was discovered. Additional nonlinear fiber-feedback was implemented that obviously provided large influence of the third order nonlinearity.

We note, that the influence of the $\chi^{(2)}$ nonlinearity in the dynamic equation for signal intensity $I_1 \propto |E_1|^2$ is proportional to $I_1 I_3$, where $I_3 \propto |E_3|^2$ (e.g. $(dI_1/dz)|_{\chi^{(2)}} \propto E_1^* E_2^* E_3 \propto |E_1|^2 |E_3|^2$, since roughly $E_2 \propto E_1^* E_3$). On the other hand, the influence of $\chi^{(3)}$ nonlinearity is proportional to I_1^2. We may state that the $\chi^{(2)}$ term is roughly linear with respect to I_1 since the pump intensity I_3 is refreshed at each round-trip. The $\chi^{(3)}$ term is nonlinear and this is crucial for the onset of chaos.

5. CONCLUSIONS

We have searched for stable operation areas of the SPOPO. From the Poincaré maps it can be seen that stable solutions are obtained either at lower pump energy or at net GDD that differs considerably from 0. The Lyapunov exponent at an unstable operation was calculated and its positive value provides an ev-

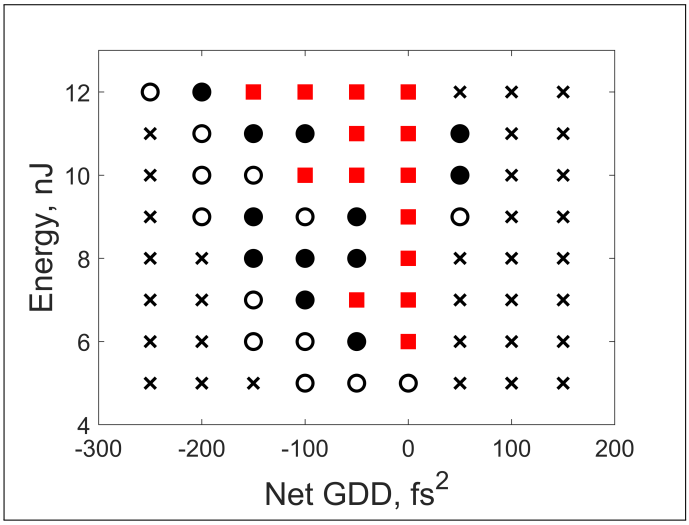

Fig. 9. (Color online) Two-parameter bifurcation diagram at $l = 0$. Crosses: stable solutions; open circles: one-period oscillations; filled circles: two-, three- and four-period oscillations; red rectangles: more than four-period oscillations and chaos.

idence of the chaos. The chaotic operation mode could not be obtained when neglecting the third-order nonlinear terms in the model equations. Without those terms, only stable solutions were obtained. At stable operation mode, the signal spectrum maximum can be shifted by varying either the resonator detuning or resonator GDD.

6. FUNDING INFORMATION

Mikas Vengris acknowledges the European Social Fund according to the activity "Improvement of researchers' qualification by implementing world-class R&D projects" of Measure No. 09.3.3-LMT-K-712, grant No. 09.3.3-LMT-K-712-0014.

7. DISCLOSURES

Disclosures. The authors declare no conflicts of interest.

REFERENCES

1. K. Ivanauskienė, I. Stasevičius, M. Vengris, and V. Sirutkaitis, "Pulse-to-pulse instabilities in synchronously pumped femtosecond optical parametric oscillator," *J. Opt. Soc. Am. B* **36**, 131–139 (2019).
2. H. M. van Driel, "Synchronously pumped optical parametric oscillators," *Appl. Phys. B* **60**, 411–420 (1995).
3. L. A. Lugiato, C. Oldano, C. Fabre, E. Giacobino, and R. J. Horowicz, "Bistability, self-pulsing and chaos in optical parametric oscillators," *Il Nuovo Cimento* **10**, 959–977 (1988).
4. D. T. Reid, "Ultra-broadband pulse evolution in optical parametric oscillators," *Opt. Express* **19**, 17979–17984 (2011).
5. P.-S. Jian, W. E. Torruellas, M. Haelterman, S. Trillo, U. Peschel, and F. Lederer, "Solitons of singly resonant optical parametric oscillators," *Opt. Lett.* **24**, 400–402 (1999).
6. B. Ruffing, A. Nebel, and R. Wallenstein, "All-solid-state cw mode-locked picosecond KTiOAsO4 (KTA) optical parametric oscillator," *Appl. Phys. B* **67**, 537–544 (1998).
7. E. Gaižauskas, R. Grigonis, and V. Sirutkaitis, "Self- and cross-modulation effects in a synchronously pumped optical parametric oscillator," *J. Opt. Soc. Am. B* **19**, 2957 (2002).
8. N. Akhmediev and A. Ankiewicz, *Dissipative solitons* (Springer, Berlin Heidelberg, 2005).
9. J. Seres and J. Hebling, "Nonstationary theory of synchronously pumped femtosecond optical parametric oscillators," *J. Opt. Soc. Am. B* **17**, 741–750 (2000).
10. R. W. Boyd, *Nonlinear optics* (Academic Press, USA, 2003).
11. D. N. Nikogosyan, *Nonlinear optical crystals* (Springer, USA, 2005).
12. R. Hamerly, A. Marandi, M. Jankowski, M. M. Fejer, Y. Yamamoto, and H. Mabuchi, "Reduced models and design principles for half-harmonic generation in synchronously pumped optical parametric oscillators," *Phys. Rev. A* **94**, 063809 (2016).
13. G. P. Agrawal, *Nonlinear fiber optics* (Academic Press, San Diego, CA, 1989).
14. M. T. Rosenstein, J. J. Collins, and C. J. De Luca, "A practical method for calculating largest Lyapunov exponents from small data sets," *Phys. D: Nonlinear Phenom.* **65**, 117–134 (1993).
15. T. Steinle, M. Floess, A. Steinmann, V. Kumar, G. Cerullo, and H. Giessen, "Stimulated Raman scattering microscopy with an all-optical modulator," *Phys. Rev. Appl.* **11**, 044081 (2019).